

RESEARCH ARTICLE | MARCH 12 2021

Thermal performance of GaInSb quantum well lasers for silicon photonics applications

C. R. Fitch; G. W. Read; I. P. Marko; ... et. al



Appl. Phys. Lett. 118, 101105 (2021)

<https://doi.org/10.1063/5.0042667>



View
Online



Export
Citation

CrossMark

Articles You May Be Interested In

GaSb-based composite quantum wells for laser diodes operating in the telecom wavelength range near 1.55- μm

Appl. Phys. Lett. (March 2015)

Room-temperature continuous-wave operation in the telecom wavelength range of GaSb-based lasers monolithically grown on Si

APL Photonics (May 2017)

p-type GaSb and $\text{Ga}_{0.8}\text{In}_{0.2}\text{Sb}$ layers grown by metalorganic vapor phase epitaxy using silane as the dopant source

Appl. Phys. Lett. (December 1996)



Time to get excited.

Lock-in Amplifiers – from DC to 8.5 GHz



Find out more



Thermal performance of GaInSb quantum well lasers for silicon photonics applications

Cite as: Appl. Phys. Lett. **118**, 101105 (2021); doi: [10.1063/5.0042667](https://doi.org/10.1063/5.0042667)

Submitted: 2 January 2021 · Accepted: 24 February 2021 ·

Published Online: 12 March 2021











View Online



Export Citation



CrossMark

C. R. Fitch,¹  G. W. Read,¹  I. P. Marko,¹  D. A. Duffy,¹  L. Cerutti,²  J.-B. Rodriguez,²  E. Tournié,² 
and S. J. Sweeney^{1,a)} 

AFFILIATIONS

¹Advanced Technology Institute and Department of Physics, University of Surrey, Guildford GU2 7HX, United Kingdom

²IES, Université de Montpellier, CNRS, F-34000 Montpellier, France

^{a)} Author to whom correspondence should be addressed: sweeney@surrey.ac.uk

ABSTRACT

A key component for the realization of silicon-photonics is an integrated laser operating in the important communication band near $1.55\ \mu\text{m}$. One approach is through the use of GaSb-based alloys, which may be grown directly on silicon. In this study, silicon-compatible strained $\text{Ga}_{0.8}\text{In}_{0.2}\text{Sb}/\text{Al}_{0.68}\text{In}_{0.32}\text{Sb}$ composite quantum well (CQW) lasers grown on GaSb substrates emitting at $1.55\ \mu\text{m}$ have been developed and investigated in terms of their thermal performance. Variable temperature and high-pressure techniques were used to investigate the influence of device design on performance. These measurements show that the temperature dependence of the devices is dominated by carrier leakage from the QW region to the X_b minima of the $\text{Al}_{0.35}\text{Ga}_{0.65}\text{As}_{0.03}\text{Sb}_{0.97}$ barrier layers accounting for up to 43% of the threshold current at room temperature. Improvement in device performance may be possible through refinements in the CQW design, while carrier confinement may be improved by optimization of the barrier layer composition. This investigation provides valuable design insights for the monolithic integration of GaSb-based lasers on silicon.

© 2021 Author(s). All article content, except where otherwise noted, is licensed under a Creative Commons Attribution (CC BY) license (<http://creativecommons.org/licenses/by/4.0/>). <https://doi.org/10.1063/5.0042667>

The realization of optoelectronic integrated circuits (OEICs) requires an efficient, silicon-compatible electrically pumped laser operating above room temperature (RT). The indirect nature of silicon makes it unsuitable as an active region. While heterogeneous integration may currently be the most advanced approach in terms of device performance,¹ the longer term goal is direct epitaxial growth of III-V lasers on silicon.¹ However, the lattice constant and thermal expansion coefficient mismatch and the polar/non-polar interface between silicon and traditional III-V laser materials causes large defect densities, leading to inefficient and unreliable lasers. Progress has been made in overcoming these challenges through the use of GaAs-based $1.3\ \mu\text{m}$ quantum dot lasers on silicon^{2,3} and Ga(NAsP)/GaP/Si quantum well (QW) lasers at $800\text{--}900\ \text{nm}$.⁴ However, an alternative material system and approach is required for long-haul telecom applications operating around $1.5\ \mu\text{m}$.

Sb-containing alloys are of interest for growth on silicon since dislocations tend to propagate parallel to the Si/III-V-Sb interface rather than into the active layers, allowing growth of high-quality active regions. GaInSb/GaSb composite quantum well (CQW) lasers have been grown by molecular beam epitaxy on 4° -off (001) silicon substrates emitting at $1.55\ \mu\text{m}$ at RT in pulsed mode,⁵ near $1.55\ \mu\text{m}$ in continuous wave (c.w.) on GaSb near RT,⁶ and more recently at

$1.59\ \mu\text{m}$ c.w. at RT on 6° miscut silicon.⁷ However, further development is needed to address high threshold current densities (J_{th}) and temperature sensitivity.⁸

To commercialize on-silicon devices, it is important to understand the efficiency limiting mechanisms of the equivalent active regions grown on GaSb. In this paper, we report on the thermal properties of GaInSb CQW devices on GaSb substrates⁶ and use a range of experimental techniques to identify the principal processes limiting device performance.¹⁶

The test devices (A, B, and C) illustrated in Fig. 1 consist of three compressively strained $\text{Ga}_{0.8}\text{In}_{0.2}\text{Sb}$ QWs. The $\text{Al}_{0.35}\text{Ga}_{0.65}\text{As}_{0.03}\text{Sb}_{0.97}$ barriers and $\text{Al}_{0.9}\text{Ga}_{0.1}\text{As}_{0.07}\text{Sb}_{0.93}$ cladding layers are lattice-matched to the GaSb substrate.

Devices B and C are CQWs formed by the insertion of one (B) and two (C) $0.45\ \text{nm}$ $\text{Al}_{0.68}\text{In}_{0.32}\text{Sb}$ barriers within each $\text{Ga}_{0.8}\text{In}_{0.2}\text{Sb}$ QW. The insertion of AlInSb monolayers into the wider wells introduces additional confinement, counteracting the reduction in bandgap caused by the additional width. Further details of the fabrication of these devices are given in Ref. 6.

Pulsed electrical injection (500 ns, 10 kHz) was used to minimize current heating effects. Device characteristics were measured as a

Material	Thickness (nm)
p-GaSb(100)	300
Graded p-AlGaAsSb	100
pAl _{0.9} Ga _{0.1} As _{0.07} Sb _{0.93}	1000
Al _{0.35} Ga _{0.65} As _{0.03} Sb _{0.97}	200
Ga _{0.8} In _{0.2} Sb	3.6 (A), 4.8 (B), 6 (C)
Al _{0.35} Ga _{0.65} As _{0.03} Sb _{0.97}	20
Ga _{0.8} In _{0.2} Sb	3.6 (A), 4.8 (B), 6 (C)
Al _{0.35} Ga _{0.65} As _{0.03} Sb _{0.97}	20
Ga _{0.8} In _{0.2} Sb	3.6 (A), 4.8 (B), 6 (C)
Al _{0.35} Ga _{0.65} As _{0.03} Sb _{0.97}	200
nAl _{0.9} Ga _{0.1} As _{0.07} Sb _{0.93}	1000
Graded n-AlGaAsSb	100
n-GaSb(100)	substrate

FIG. 1. Test device structures.

function of temperature from 40 to 300 K using a closed-cycle cryostat system. Figure 2(a) shows the facet output intensity (I) variation with current density (J) and temperature (T) for representative device B. Figure 2(b) shows the extracted J_{th} variation with temperature for all three devices.

For these lattice-matched devices, defect-related recombination is assumed to be negligible in the QW region and at low temperatures, where J_{th} is low, other forms of non-radiative recombination are also assumed negligible. For an ideal QW laser at low temperatures, the radiative component of threshold current density, $J_{rad} \propto T^9$, and for our devices J_{rad} can be seen to dominate threshold below ~ 150 K.

The J_{rad} components at RT were approximated by linear extrapolation of the low temperature J_{th} to 300 K shown as the shaded area in Figure 2(b) and in Table I.

For $T > 150$ K, J_{th} increases super-linearly, suggesting the onset of non-radiative processes such as Auger recombination or carrier leakage consistent with evidence from other laser types at this wavelength.¹⁰

In a simple model, J_{th} can be expressed as¹⁶

$$J_{th} = eL_z(A n + B n^2 + C n^3) + J_{leak}, \quad (1)$$

where e is the electronic charge, L_z is the active layer thickness, n is the carrier density (assuming equal electron and hole carrier densities), and A , B , and C are the recombination coefficients for defect, radiative, and Auger recombination, respectively. The J_{leak} term accounts for carrier leakage from the QWs.

Auger recombination and carrier leakage are strongly temperature-dependent, which may explain the strong increase in J_{th} with temperature.¹¹ The reduction in J_{th} at RT from device structures A to B to C may be attributed to the increased gain volume, which reduces the threshold carrier density, n_{th} , by lowering the band filling and increasing the photon generation rate for a given injection current.

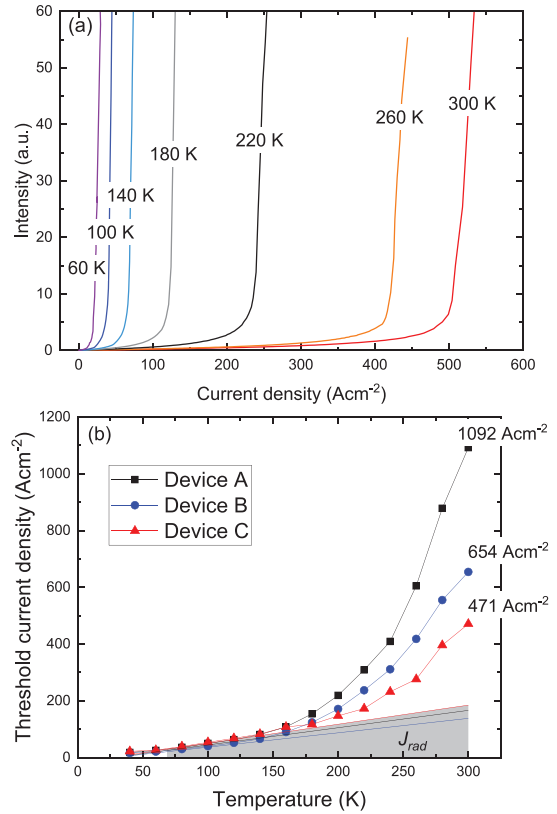


FIG. 2. (a) Temperature-dependent LI (device B); and (b) threshold current densities and radiative components (all devices).

TABLE I. Threshold current densities and radiative components at 300 K.

	Device A	Device B	Device C
J_{th} (Acm ⁻²)	1092	654	471
J_{rad} (Acm ⁻²)	170 ± 6	147 ± 10	189 ± 5
J_{rad}/J_{th} (%)	15 ± 1	23 ± 2	40 ± 1

Increased optical confinement would also contribute to the reduction in n_{th} by increasing modal gain and the stimulated emission rate.

Approaching room temperature J_{th} increases exponentially and, over a limited temperature range, this increase may be described by the characteristic temperature T_0 :¹²

$$T_0 = \left(\frac{d \ln(J_{th})}{dT} \right)^{-1} = \left(\frac{1}{J_{th}} \frac{dJ_{th}}{dT} \right)^{-1}. \quad (2)$$

A higher T_0 is desirable as it corresponds to greater thermal stability of J_{th} . Expressions for the characteristic temperature due to radiative, Auger recombination, and leakage effects can be derived as¹²

$$T_0(I_{rad}) = \frac{T}{1 + 2x}, \quad (3)$$

$$T_0(I_{Aug}) = \frac{T}{3 + \left(\frac{E_a}{kT}\right) + 3x}, \quad (4)$$

$$T_0(I_{leak}) = \frac{T}{\left(\frac{E_a}{kT}\right)}, \quad (5)$$

where x is a “non-ideality” factor, e.g., due to optical losses, and E_a is the respective activation energy for the Auger or leakage process.

The theoretical variation of $T_0(T)$ for J_{th} can be written as a weighted average of the individual T_0 values:

$$\frac{1}{T_0} = \frac{1}{T_{0(rad)}} R + \frac{1}{T_{0(nonrad)}} (1 - R), \quad (6)$$

where $R(T)$ is defined as J_{rad}/J_{th} and $T_{0(nonrad)}$ corresponds to either the Auger or leakage process. $T_0(T)$ was measured using a five-point average and compared with a numerical model to investigate the non-radiative contribution to J_{th} .

Figure 3(a) shows the measured and modeled $T_0(T)$ for all three devices for radiative recombination and carrier leakage together with the radiative and leakage limits for device B as an example. Figure 3(b) shows that a similarly good fit may be achieved assuming radiative and Auger recombination. At low temperatures, T_0 tends toward the radiative limits, while above a break-point temperature, T_B ,¹⁶ it tends

toward the leakage or Auger limits. The difference in $T_0(T)$ between the three structures is consistent with the trends in J_{th} and highlights the improvement in performance with increasing composite well thickness where a lower n_{th} leads to a reduction in non-radiative recombination. Figures 3(c) and 3(d) show the example of the measured J_{th} for device B and the result of fitting the radiative and leakage (a) or radiative and Auger (b) components from the T_0 model. A similar quality of fit is found for devices A and C. The T_0 data may, therefore, be explained by considering either leakage or Auger recombination although it is not possible to distinguish which is dominant from this analysis alone.

Using a similar approach, we investigated the temperature sensitivity of the differential quantum efficiency (slope) above threshold, η_d , where

$$\eta_d \propto \frac{dL}{dI}. \quad (7)$$

The characteristic temperature T_1 is defined as $\eta_d(T) = \eta_0 \exp(-T/T_1)$, where η_0 is a constant,¹³ so

$$T_1 = -\left(\frac{d \ln(\eta_d)}{dT}\right)^{-1} = -\left(\frac{1}{\eta_d} \frac{d\eta_d}{dT}\right)^{-1}. \quad (8)$$

Equation (8) was applied using a three-point average to plot the experimental values of T_1 .

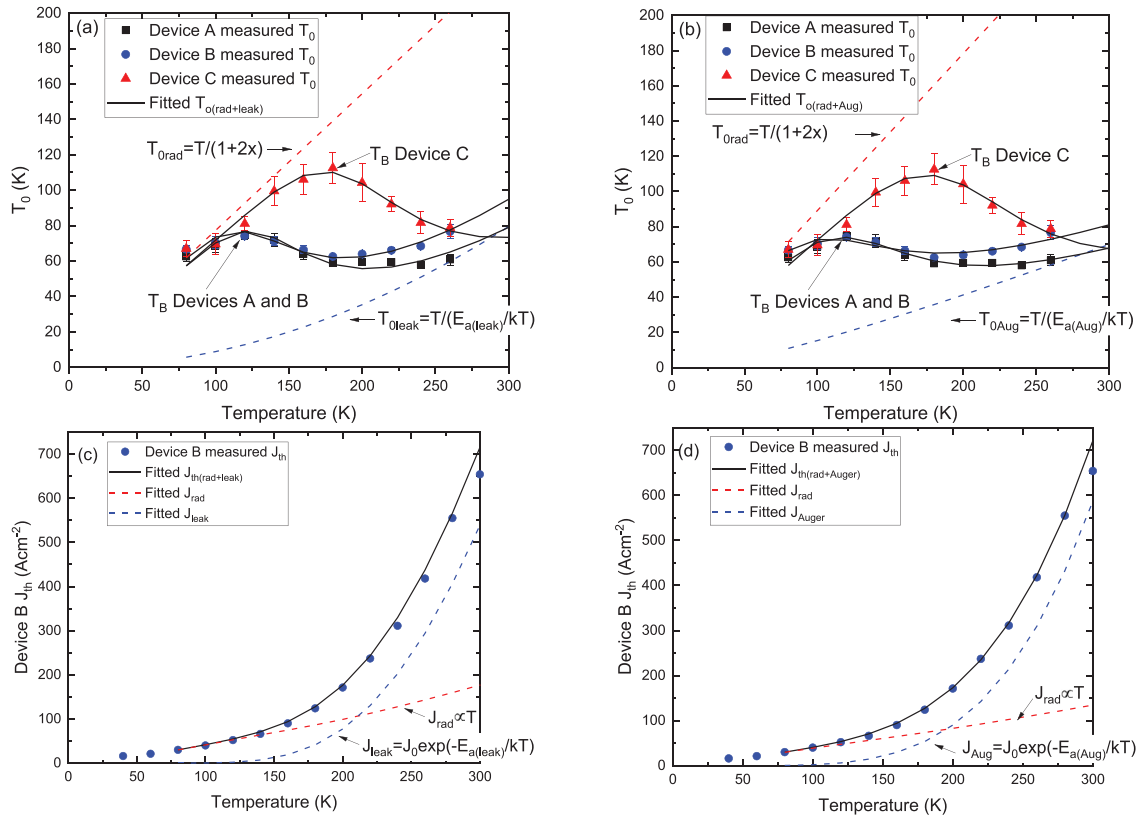


FIG. 3. Experimental and modeled characteristic temperature and threshold current density (a) T_0 (I_{rad} and I_{leak}), (b) T_0 (I_{rad} and I_{Auger}), (c) J_{th} (J_{rad} and J_{leak}), and (d) J_{th} (J_{rad} and J_{Auger}).

The differential quantum efficiency η_d may be expressed as

$$\eta_d = \eta_i \frac{\alpha_m}{\alpha_i + \alpha_m} \quad (9)$$

Here, η_i is the internal quantum efficiency, α_i is the internal loss, and α_m is the mirror loss expressed as

$$\alpha_m = \frac{1}{L_{cav}} \ln \frac{1}{R_f}, \quad (10)$$

where L_{cav} is the cavity length and R_f is the as-cleaved facet reflectivity. Assuming the change in α_m with temperature is negligible, we deduce that

$$T_1 = \frac{1}{\frac{1}{\alpha_i + \alpha_m} \frac{d\alpha_i}{dT} - \frac{1}{\eta_i} \frac{d\eta_i}{dT}} \quad (11)$$

Terms on the left-hand side of the denominator are related to cavity losses and on the right-hand side to injection losses (e.g., carrier leakage). This decomposition allows investigation of the relative contributions to T_1 . We used a least squares numerical fit model to vary $d\alpha_i/dT$ and $d\eta_i/dT$ to fit to the measured $\eta_d(T)$ using Eq. (11).

Figure 4(a) shows the relative change in slope efficiency η_d for all three device structures. Figure 4(b) shows the measured and modeled average T_1 values. The limits associated with varying only α_i or η_i with temperature are also shown.

From this fit, it is clear that $d\eta_i/dT$ dominates with $d\alpha_i/dT$ having a negligible effect. This confirms that the temperature sensitivity of T_1 is due to injection rather than optical losses and supports the T_0 analysis, which identified carrier leakage as a possible contributory factor. It also indicates that Inter Valence Band Absorption (IVBA) and Free Carrier Absorption (FCA) are not significant because they are associated with the α_i rather than the η_i contribution to η_d . Auger recombination is not expected to influence the T_1 analysis since n is (ideally) pinned above threshold. An important outcome of the T_1 analysis is that the efficiency data can only be explained by the presence of carrier leakage.

Both carrier leakage and Auger recombination are sensitive to the band structure. Hydrostatic pressure can be used to reversibly change the band structure of a semiconductor; hence, it was used to assess the dependence of the device performance on the band structure. Pressures up to 400 MPa were applied using a Unipress helium compressor system, details of which may be found in Ref. 11.

The measured variation of J_{th} with pressure is shown in Fig. 5(a).

A numerical model was created to describe how Auger recombination and carrier leakage vary with pressure to investigate their quality of fit to the experimental data.

In an ideal QW laser, where optical losses are negligible, J_{rad} scales with bandgap according to $J_{rad} \propto E_g^2$.

The pressure dependence of the leakage and Auger components takes the form

$$J_{nonrad} = J_0 \exp \left[- \left(\frac{dE_a}{dP} \right) \frac{P}{k_b T} \right], \quad (12)$$

where $J_0 = 1$ for normalized data and dE_a/dP is the net change in the respective activation energy with pressure.

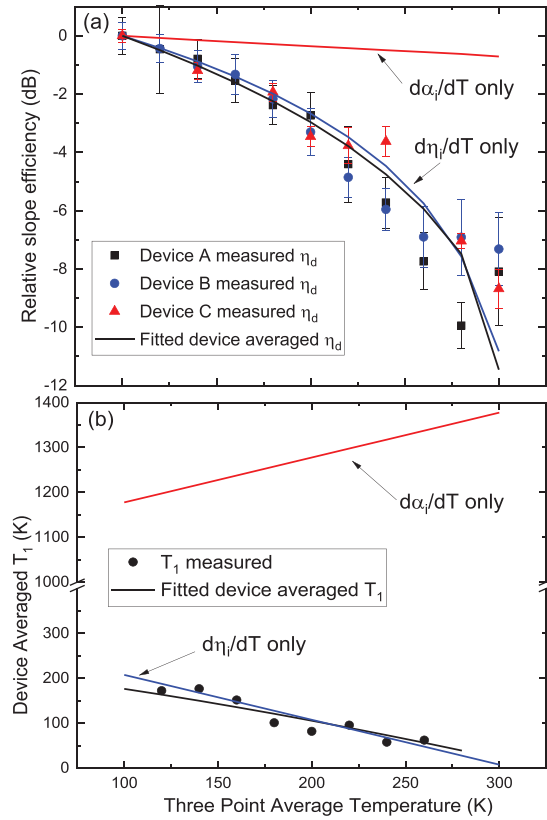


FIG. 4. Experimental and modeled slope efficiency (a) and characteristic temperature T_1 (b).

For leakage, dE_a/dP corresponds to the net change in band alignment between the quasi-Fermi level in the conduction band, taken to be equal to the QW electron ground state (e_i), and the energy of the states into which the carriers escape. We assume that e_i changes as dE_{lase}/dP and the valence band alignment is approximately pressure independent.¹⁴ dE_{lase}/dP was measured to be ~ 6 meV kbar⁻¹ for all three devices.

CHSH Auger recombination (where the energy of a Conduction band electron recombining with a hole in the Heavy hole band is given to a third hole in the Heavy hole band that is excited into the spin split-off band) is sensitive to the difference between the bandgap (E_g) and the spin-orbit (SO) split-off-energy (Δ_{SO}). For our devices where $E_g > \Delta_{SO}$, the CHSH activation energy is given by

$$E_a(CHSH) = \frac{m_{so}}{2m_h + m_c - m_{so}} (E_g - \Delta_{SO}), \quad (13)$$

where m_c and m_h are the electron and heavy hole band, in-plane, effective masses and m_{so} is the SO split-off band effective mass.

The CHCC Auger activation energy is

$$E_a(CHCC) = \frac{m_c}{m_c + m_h} E_g. \quad (14)$$

CHCC refers to electron-hole recombination between the Conduction and Heavy hole bands accompanied by excitation of a Conduction band electron further into the Conduction band.

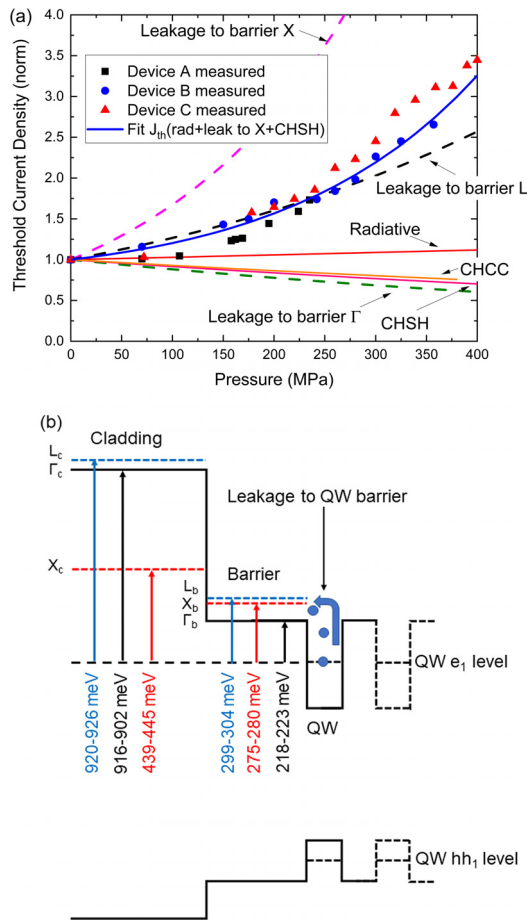


FIG. 5. (a) Threshold current density variation with pressure - Experimental measurements (solid symbols) and theoretical dependence of the individual current paths and best fit with pressure (device B) (b) schematic band alignment.

In (13) and (14), E_g changes according to dE_{lase}/dP . From $k.p$ theory, m_c and m_{so} increase approximately proportionally to the bandgap, and hence pressure, while m_h is relatively independent of pressure.¹⁵ QW effective masses were calculated from a linear interpolation of the binary components from Vurgaftman *et al.*¹⁶ Other Auger processes have been ignored since they have previously been shown to be relatively weak.^{10,17} Due to the closeness of the e_1 and Δ_{SO} energies, CHSH is expected to dominate the Auger current at wavelengths $< 2 \mu\text{m}$.¹⁸

An increasing J_{th} with pressure is generally a strong indicator of carrier leakage from the QW to the indirect X or L valleys. In contrast, J_{th} decreases with pressure for CHSH/CHCC Auger processes or for leakage from the QW to the barrier Γ_b band edge (when the barrier Γ_b band edge pressure coefficient is smaller than the QW, as here).

The QW e_1 to barrier Γ_b , X_b , and L_b minima energy offsets were calculated at RT and ambient pressure for the three structures by combining the binary energy gaps, bowing parameters, and valence band offsets from Vurgaftman *et al.*,¹⁶ accounting for strain in the QW.

For the three structures, the range of values are e_1 - Γ_b = 218–223 meV; e_1 - X_b = 275–280 meV; and e_1 - L_b = 299–304 meV

(e_1 -cladding separations were all > 439 meV), Fig. 5(b). While these energy offsets should be sufficient to confine the majority of carriers, the Fermi-Dirac distribution of carriers extends into these energies where there is a high density of states, hence increasing the recombination rate. It was also found that the energy offsets and configuration of the barrier minima are very sensitive to the bowing parameters, which vary considerably in the literature.^{16,19}

As evident from Fig. 5(a), the increase in J_{th} with pressure is stronger than that expected for leakage to the L_b -valley states. However, it is consistent with leakage to the X_b -valley dominating the increase in J_{th} . A good fit to the experimental results was achieved for all devices using a combination of radiative recombination, leakage to the barrier X_b minima (forming up to 43% of J_{th}), and a contribution of CHSH/CHCC Auger recombination or leakage to the barrier Γ_b or L_b minima. Shockley-Read-Hall (SRH) is likely to be a strong factor in the subsequent recombination of carriers in the barrier material.

The results of this study demonstrate the potential of GaSb-based QW lasers for silicon photonics applications in the telecom wavelength range and opportunities for ongoing improvement.

We showed that the strong temperature sensitivity of J_{th} could be explained by either leakage or Auger recombination. However, the temperature sensitivity of η_d was found to be dominated by carrier injection, confirming that leakage must be present. Furthermore, from pressure-dependent measurements, carrier leakage from the QW active region to the barrier X_b valley states was found to be a key limiting factor in the performance of these devices. This could be reduced by increasing the activation energy of the leakage paths by a small increase in the lattice matched barrier Al and As fractions and without compromising optical confinement provided by the cladding. Further improvement in reducing J_{th} and thermal sensitivity might also be achieved by increasing the number of QWs although the relatively small improvements associated with increased gain volume of device C over B compared with B over A suggest diminishing scope for improvement. Optimization would also benefit from a detailed investigation of bowing parameters and band alignments in this system.

This work was partly supported by EPSRC (UK) under grant EP/N021037/1, a SEPnet Ph.D. scholarship for D. A. Duffy, the French ANR (*Project OPTOSi*, No. ANR-12-BS03-002), and by the French “Investment for the Future” program (*EquipEx EXTRA*, No. ANR-11-EQPX-0016).

DATA AVAILABILITY

The data associated with this work are openly available at Zenodo, <https://doi.org/10.5281/zenodo.4353309>, Ref. 20.

REFERENCES

- C. Cornet, Y. Leger, and C. Robert, *Integrated Lasers on Silicon* (ISTE Press, 2016).
- M. Liao, S. Chen, S. Chen, S. Huo, J. Wu, M. Tang, K. Kennedy, W. Li, S. Kumar, M. Martin, T. Baron, C. Jin, I. Ross, A. Seeds, and H. Liu, *IEEE J. Sel. Top. Quantum Electron.* **23**, 1 (2017).
- D. Jung, Z. Zhang, J. Norman, R. Herrick, M. J. Kennedy, P. Patel, K. Turnlund, C. Jan, Y. Wan, A. C. Gossard, and J. E. Bowers, *ACS Photonics* **5**, 1094 (2018).
- S. Liebich, M. Zimprich, P. Ludewig, A. Beyer, K. Volz, W. Stolz, B. Kunert, N. Hossain, S. R. Jin, and S. J. Sweeney, in *Proceedings 22nd IEEE International Semiconductor Laser Conference* (2010), Vol. 143.

- ⁵L. Cerutti, J. B. Rodriguez, and E. Tournié, *IEEE Photonics Technol. Lett.* **22**, 553 (2010).
- ⁶L. Cerutti, A. Castellano, J. B. Rodriguez, M. Bahri, L. Largeau, A. Balocchi, K. Madiomanana, F. Lelarge, G. Patriarche, and E. Tournié, *Appl. Phys. Lett.* **106**, 101102 (2015).
- ⁷A. Castellano, L. Cerutti, J. B. Rodriguez, G. Narcy, A. Garreau, F. Lelarge, and E. Tournié, *APL Photonics* **2**, 061301 (2017).
- ⁸E. Tournié, A. Castellano, K. Madiomanana, G. Narcy, A. Garreau, F. Lelarge, J.-B. Rodriguez, and L. Cerutti, “GaSb lasers grown on silicon substrate for telecom applications,” in *Molecular Beam Epitaxy, From Research to Mass Production*, 2nd ed., edited by M. Henini (Elsevier, 2018), Chap. 27. pp. 625–635.
- ⁹P. Blood, *Quantum Confined Laser Devices*, 1st ed. (Oxford University Press, 2015).
- ¹⁰S. R. Jin, S. J. Sweeney, S. Tomić, A. R. Adams, and H. Riechert, *IEEE J. Sel. Top. Quantum Electron.* **9**, 1196 (2003).
- ¹¹A. F. Phillips, S. J. Sweeney, A. R. Adams, and P. J. A. Thijs, *IEEE J. Sel. Top. Quantum Electron.* **5**, 401 (1999).
- ¹²E. P. O'Reilly and M. Silver, *Appl. Phys. Lett.* **63**, 3318 (1993).
- ¹³N. Tansu, Y. L. Chang, T. Takeuchi, D. P. Bour, S. W. Corzine, M. R. T. Tan, and L. J. Mawst, *IEEE J. Quantum Electron.* **38**, 640 (2002).
- ¹⁴W. Mönch, *Electronic Properties of Semiconductor Interfaces*, Springer Series in Surface Sciences Book Series Vol. 43 (SSSUR, 2004).
- ¹⁵A. Krier, X. L. Huang, and V. V. Sherstnev, *Mid-Infrared Semiconductor Optoelectronics*, Springer Series in Optical Sciences Book Series Vol. 118 (SSOS, 2006).
- ¹⁶I. Vurgaftman, J. R. Meyer, and L. R. Ram-Mohan, *J. Appl. Phys.* **89**, 5815 (2001).
- ¹⁷A. Sugimura, *IEEE J. Quantum Electron.* **19**, 930 (1983).
- ¹⁸S. J. Sweeney, G. Knowles, T. E. Sale, and A. R. Adams, *Phys. Status Solidi B* **223**, 567 (2001).
- ¹⁹S. Adachi, *Properties of Semiconductor Alloys: Group-IV, III-V and II-VI Semiconductors*, Wiley Series in Materials for Electronic & Optoelectronic Applications (John Wiley & Sons, Ltd., 2009).
- ²⁰C. R. Fitch, G. W. Read, I. P. Marko, D. A. Duffy, L. Cerutti, J.-B. Rodriguez, E. Tournié, and S. J. Sweeney (2020). “Thermal performance of GaInSb quantum well lasers for silicon photonics applications.” Zenodo. <https://zenodo.org/record/4353309#.YEFvn1GWy3A>.